ECOLOGICAL ENGINEERING & ENVIRONMENTAL TECHNOLOGY

Ecological Engineering & Environmental Technology, 2026, 27(10), 61–81
https://doi.org/10.12912/27197050/226297
ISSN 2719–7050, License CC-BY 4.0

Received: 2026.07.17
Accepted: 2026.08.23
Published: 2026.09.10

Development of a 30 m spatiotemporal land use and land cover dataset (1985–2025) for the Allal El Fassi Watershed (Morocco) using Landsat time series and Google Earth Engine

Otmane Bensouda Mourri[1,2*], Mohamed Baaba[2], Abdelkarim Ouallal[2], Ayyoub Khazaza[2,3], Ferdaouss Lakhili[2], Fahed El Amarty[1,2,4], Lahcen Benaabidate[1]

[1] Laboratory of Geo-Resources and Environment (LGRE), Faculty of Sciences and Technologies of Fez, Sidi Mohammed Ben Abdellah University, Route d'Immouzzer, BP 2202, Fez, Morocco
[2] National Agency for Water and Forests (ANEF), DPANEF Sefrou, Morocco
[3] Functional Ecology and Environmental Engineering Laboratory (LEFGE), FST-Fes, Sidi Mohammed Ben Abdellah University, Immouzer Road, BP: 2202, Fez 30000, Morocco
[4] Laboratory of Intelligent Systems, Energy, and Sustainable Development (SIEDD), Private University of Fez, Lotissement Quaraouiyine Route Ain Chkef, Fès 30000, Morocco
* Corresponding author's e-mail: otmane.bensoudamourri@usmba.ac.ma

ABSTRACT

Understanding environmental changes and promoting the sustainable management of watersheds requires long-term monitoring of land use and land cover (LULC), especially in Mediterranean regions subject to high climate variability and growing anthropogenic pressure. Using the whole Landsat imagery archive accessible via the Google Earth Engine platform, this study introduces a novel spatiotemporal land use and land cover dataset (LULC_AllalElFassi) for the Allal El Fassi Watershed spanning the years 1985–2025. The methodology ensures the geographical and temporal coherence of the produced maps while detecting changes in land use and land cover by combining a locally adaptive classification strategy with the Continuous Change Detection and Classification (CCDC) algorithm. Eight land use and land cover classifications could be mapped at a spatial resolution of 30 m thanks to the dataset, which was created using 2000 training samples and 800 independent validation points. The total accuracy of the results was 82.8282.82±0.45 percentage points. Water bodies (93.65%), built-up areas (92.65%), agricultural land (87.64%), and dense woods (87.81%) had especially good categorization accuracy. Long-term landscape dynamics investigation showed a significant increase in open forests (+898.50%), a notable expansion of agricultural land (+10.38%) and built-up areas (+789.63%), and a decrease in thick forests (−9.35%) and herbaceous and poorly vegetated regions (−4.73%). These alterations show that the forest canopy is gradually opening, agricultural production is becoming more intensive, and urbanization is increasing across the watershed. The suggested dataset is a useful decision-support tool for hydrological modeling, water erosion assessment, forest resource management, and sustainable planning of Mediterranean watersheds. It also provides a reliable data source for long-term environmental monitoring.

Keywords: land use/land cover dynamics, Continuous Change Detection and Classification, Google Earth Engine, Landsat time series, spatiotemporal mapping, Allal Fassi Watershed, watershed monitoring.

INTRODUCTION

Land use and land cover (LULC) are among the most important drivers of environmental change worldwide. This is because human behavior is strongly intertwined with natural processes, and these are the most complex ones, like climate change, urbanization, agricultural growth, and resource use. By altering hydrological cycles, energy balances, biodiversity, carbon storage, and ecosystem services delivery levels, such changes can profoundly change how ecosystems operate (Cerdan et al., 2010; García-Ruiz et al., 2017; Gorelick et al., 2017). The combination of high climate variability and increasing human pressure on natural resources is what makes these dynamics especially evident in Mediterranean regions. These areas are now regarded as the hotspots of climate change worldwide.

Clarifying how land degradation operates and predicting its effects on water resources in a watershed requires understanding of land-use and land-cover changes. Changes in plant cover directly affect surface runoff, water erosion, groundwater recharge, sediment transport, and surface water quality (Panagos et al., 2015; Gorelick et al., 2017; Bengtsson et al., 2019; Borrelli et al., 2020). Similarly, the deterioration of forest ecosystems, the growth of urban areas, and the expansion of agricultural operations all increase watersheds' susceptibility to environmental threats. Therefore, a basic requirement for creating efficient natural resource management plans and climate change adaptation strategies is the availability of trustworthy long-term land-use and land-cover time series (García-Ruiz et al., 2017; Gorelick et al., 2017).

As of the last 20 years with the development of satellite remote sensing has considerably improved land use and land cover. For example, the Landsat program provides a continuous archive of satellite images at a geographical resolution of 30 m and therefore this is an opportunity to study long-term changes of the environment (Andreu et al., 1998; El Amarty, Lahrach, et al., 2024; El Amarty, Chakir, et al., 2024; Amarty et al., 2025). The large-scale processing of satellite image time series at regional and national scales has gotten easier by the rise of cloud-based computing platforms such as Google Earth Engine. However, LULC products are still based on an independent classification method for each observation date, which may produce temporal inconsistencies and mistakes in classification (Zhu and Woodcock, 2014; Bai et al., 2020; Xu and Somers, 2021; Pratson et al., 2023).

New methods based on continuous time-series analysis have been created to get around these restrictions. Among these, Zhu and Woodcock's (2014) Continuous Change Detection and Classification (CCDC) algorithm automatically identifies temporal breakpoints, updates land use and land cover changes over time, and models the spectral trajectory of each pixel using the entire archive of available Landsat observations (Patel et al., 2015; Soulard et al., 2016; Gorelick et al., 2017; Claverie et al., 2018; Weiss et al., 2020; Tamiminia et al., 2020). This method is becoming more and more popular for creating long-term historical land use and land cover datasets because it greatly increases the temporal consistency of LULC classifications while lowering the errors associated with traditional classification techniques (Zhu and Woodcock, 2014; Zhu, 2017; Wulder et al., 2019).

High-spatial-resolution land use and land cover monitoring products are still hard to come by at the size of Mediterranean watersheds, especially in Morocco, despite these methodological advancements. Current databases, which are often created at national or continental scales, frequently fall short of adequately representing the transitions between the many vegetation cover types typical of Mediterranean ecosystems or capturing local landscape characteristics (Cammeraat and Imeson, 1999; Cosandey et al., 2005; Boellstorff and Benito, 2005; Bellin et al., 2009). This restriction makes it difficult to analyze the trajectories of landscape change and to evaluate how changes in land use and land cover affect forest ecosystems, water resources, and land-use planning regulations.

Such challenges are reflected in the Allal El Fassi Dam watershed located in the Moroccan Middle Atlas. This watershed is crucial for the conservation and management of forest ecosystems, drinking water, and irrigation. But the growth of agriculture, pressure on forest ecosystems, urbanization, and climate change in the last decades have all contributed to sudden changes in the landscape. In order to better manage watersheds and to improve land planning, we need to understand these changes in detail. LULC_AllalElFassi is a new land use and land-cover dataset that spans 1985 to 2025 with a spatial resolution of 30 m. The dataset is generated using the CCDC algorithm and the Landsat archive available online using Google Earth Engine. It comprises 26 observation dates and a classification system for Mediterranean landscapes with eight land use and land cover classes.

The scientific contribution in this work is not that of developing a new change detection algorithm, as the CCDC framework has already been developed and applied in a few papers. The originality of the proposed approach is that it draws on several aspects in a watershed-scale map. These components include: first, using the full Landsat archive to reconstruct a 26-date spatiotemporal LULC dataset covering the period 1985–2025; second, developing an eight-class classification scheme with particular focus on ecology, landscape, and hydro-sedimentary characteristics of a Mediterranean watershed; third, generating spatio-temporally stable training data with the help of the CCDC stability information; fourth, using a locally adaptive classification scheme in which only changed pixels are classified; and fifth, applying a spatio-temporal consistency optimization method to reduce false transitions between successive maps. To the best of our knowledge, LULC_AllalElFassi is the first 30 m, eight-class long-term LULC dataset developed for the Allal El Fassi watershed between 1985 and 2025.

This study aims to:

- produce a multi-temporal land use and land cover dataset spanning the period 1985–2025 for the Allal El Fassi Watershed;
- identify and analyze the major changes in the eight land use and land cover classes;
- determine the thematic and temporal reliability of the data using independent reference data and uncertainty-related accuracy measures;
- and produce a reliable watershed-scale mapping framework and an open dataset for environmental monitoring and sustainable resource management in Mediterranean regions.

METHODS AND MATERIALS

The area study

The Allal El Fassi watershed is located in the hilly Middle Atlas region of northern Morocco, in the eastern part of the Sebou River Basin (Figure 1). It channeled the runoff from the Atlas Mountains into the Allal El Fassi Dam, a critical hydraulic structure for water supply, irrigation and to water and plants. As one of the main sub-watersheds of the Sebou Basin, the Allal El Fassi watershed covers approximately 5227 km² and forms part of a hydrographic system (El Amarty et al., 2025; Hasnae et al., 2026; Hattafi et al., 2026; Fikri et al., 2026; Lakhili et al.).

The watershed is characterized by large geographic variation, ranging from lowland plains in the downstream areas to the mountains of the Middle Atlas, where the elevation at sea level is more than 2000 meters. This range of characteristics affects the structure of the drainage network, the surface runoff and the placement of vegetation types, land use and land cover types. The watershed is situated in the Middle Atlas structure and is made up mostly of marl, Quaternary alluvial deposits in the valley bottom and Jurassic carbonate (limestones and dolomites). As well as influencing soil distribution and ecology, this variety of properties is also responsible for infiltration, surface runoff and erosion.

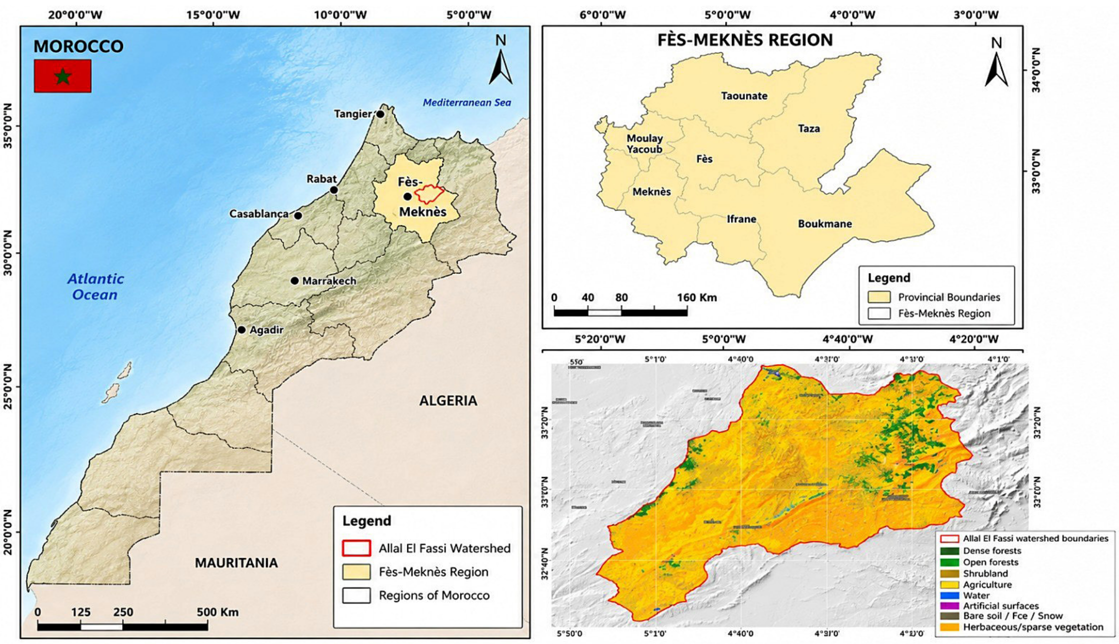

Figure 1. Allal El Fassi Watershed location

Datasets

Landsat time series, a reference dataset for model training, and an independent dataset for accuracy evaluation are all taken into consideration to create the LULC_AllalElFassi dataset. Google Earth Engine was used to collect all Landsat images from 1984 to 2025. The Landsat 5 Thematic Mapper (TM), Landsat 7 Enhanced Thematic Mapper Plus (ETM+), Landsat 8 operational land imager (OLI), and Landsat 9 OLI sensors were all used to collect the data. The Landsat Ecosystem Disturbance Adaptive Processing System (LEDAPS) algorithms for Landsat 5 and 7 and Land Surface Reflectance Code (LaSRC) algorithms for Landsat 8 and 9 were applied to transform all the images to surface reflectance to obtain a consistent time series. The relative radiometric normalization, based on the cross-sensor harmonization coefficients proposed by Roy et al. (2014), was then used to adjust for radiometric differences among the TM, ETM+, and OLI sensors.

The reference land use and land cover dataset for 2020 was created by analyzing Landsat false-color composites and spectral time series, as well as visually interpreting extremely high-resolution imagery from Google Earth Pro. A stratified sampling technique was used to choose 2000 training samples in order to represent the watershed's spatial and spectral diversity. Eight land use and land cover types make up the classification scheme: dense forests (DF), which are closed forest stands dominated by *Quercus rotundifolia* and *Cedrus atlantica*; Water bodies (WTR), such as the Allal El Fassi Reservoir and the permanent river network; shrublands (SHR); herbaceous and sparse vegetation (HSV); croplands (CRP), including rainfed and irrigated crops as well as fallow land; impervious surfaces (IMP); and bare land, ice, and snow (BAL). A more open tree canopy distinguishes open forests (OF). This comprehensive classification system provides a suitable foundation for water erosion assessment and reservoir sedimentation risk analysis by enabling a more accurate discrimination of land surface conditions involved in hydrological and erosion processes, particularly shrublands, herbaceous vegetation, and bare land.

An independent validation dataset with 800 reference points was used to evaluate the final dataset's correctness. To ensure fair representation of the eight land-use and land-cover classifications, these locations were selected through stratified random sampling. Google Earth Pro's extremely high-resolution imagery was visually interpreted to establish the reference class assigned to each place. When needed, Landsat time series analysis and contextual data were included. The accuracy evaluation was independent because the validation dataset did not contain any of the samples utilized for model training.

Methodology

The LULC_AllalElFassi product comprises 26 land use and land cover maps for 1985–2025, with three five-year reference dates (1985, 1990 and 1995) and annual maps from 2000 to 2025. The five-year intervals before 2000 reflect the limited availability of cloud-free Landsat observations during the early years of the archive, and the denser Landsat record after 2000 allowed for LULC mapping annually.

The methodology combines the CCDC algorithm proposed by Zhu and Woodcock (2014) with a locally adaptive updating procedure to generate a multi-date LULC dataset over time using the different LULC data sets. The CCDC algorithm is used to identify breakpoints in the spectral trajectories of individual pixels and detects land-cover changes throughout the Landsat archive. The locally adaptive updating procedure then assigns the most appropriate LULC class to each detected change and performs a spatio-temporal consistency optimization to reduce unrealistic transitions and improve the spatial and temporal coherence of the LULC maps. The entire process is shown in Figure 2.

There are four main steps in the methodology shown in Figure 2. Using Landsat time series, the first step is to identify temporally stable pixels and catch sudden breakpoints in the spectral paths of modified pixels. The second step is to connect the reference land use and land cover data to the temporal stability masks in an attempt to generate spatiotemporally stable training data. To assign new land-use and land cover classes to pixels which we have seen have changed, the third stage is to develop locally adaptive classification models. Finally, we apply spatiotemporal consistency optimization to avoid false change detection and have no inconsistencies between subsequent maps.

For the time series, low quality Landsat data was removed before change detection. CFmask method was used to mask clouds, cloud shadows, saturated pixels and data gaps due to a loss of

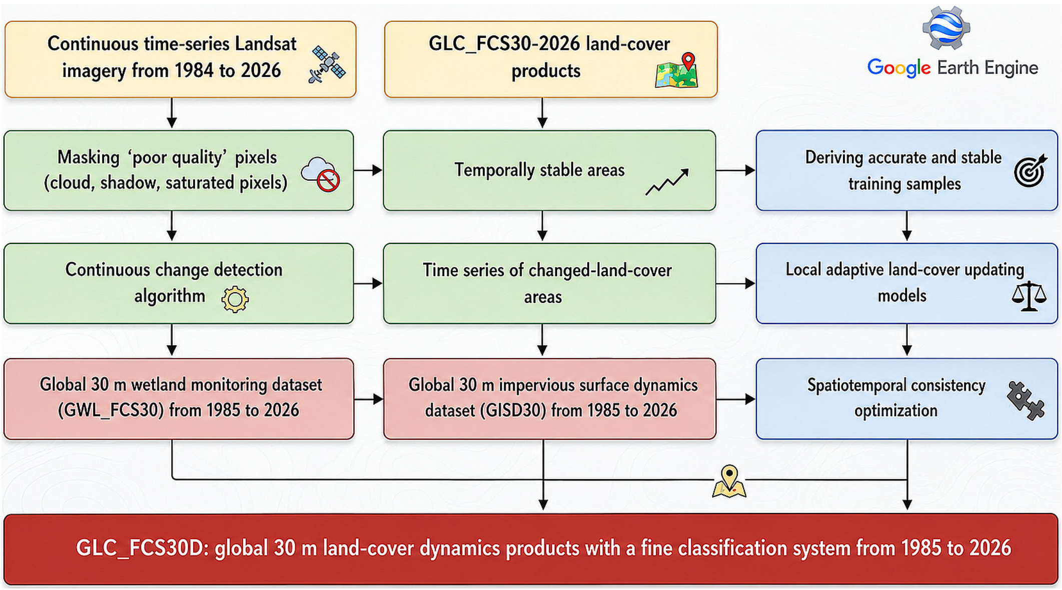

Figure 2. Workflow of the proposed methodology combining the Continuous Change Detection and Classification algorithm with a local adaptive updating procedure

the Scan Line Corrector (SLC) in Landsat 7. The U.S. Geological Survey (USGS) has used this algorithm to identify clouds and cloud shadows in Landsat images, obtaining 96.4% of the total accuracy (Zhu and Woodcock, 2014b; Zhu, 2017a; Wulder et al., 2019). Tmask (multiTemporal mask) used to detect polluted pixels was also used to detect less polluted pixels and haze in the time series with temporal information from cloud-free observations (Zhu and Woodcock, 2014b). The Google Earth Engine platform's CCDC algorithm can take into account this. The reliability of breakpoint detection was improved, and the impact of low-quality observations on time-series modeling was reduced by applying these preprocessing steps sequentially.

The entire Google Earth Engine (GEE) process was performed in a sequence to ensure that the final dataset could be reproduced. First, Landsat Collection 2 Surface Reflectance images were taken and harmonized to minimize radiometric differences among the TM, ETM+ and OLI sensors. Clouds, cloud shadows, saturated pixels, snow and Landsat-7 SLC-off gaps were removed by the CFMask algorithm along with the TMask procedure. The time series were then analysed by the CCDC algorithm to see time breakpoints and stable pixels. Finally, spatio-temporally stable training samples were generated by combining the reference dataset with the CCDC stability masks. The spectral, phenological, textural and topographic predictor variables were obtained and used to train locally adaptive Random Forest classifiers. Only pixels that were changed were reclassified and a spatiotemporal consistency optimization was applied to minimize misclassifications and to keep time consistency between 1985 and 2025.

LULC_AllalElFassi classification system

The first step in mapping and monitoring land use and land cover is to define the classification scheme. Here a system was developed to describe the hydro-sedimentary, biological and landscape characteristics of the Allal El Fassi watershed. Eight land cover and land use types were identified.

Closed forest formations with a continuous tree canopy and canopy cover greater than 40% are called DF. They are mostly made up of holm oak (*Quercus rotundifolia*) and Atlas cedar (*Cedrus atlantica*) stands. Open woodland formations with 15% to 40% canopy coverage are termed OF. Shrublands (SHR) are vegetation communities in which Mediterranean matorral formations and shrubs dominate. Grasslands, perennial herbaceous communities and poorly vegetated areas are classified as herbaceous and sparse vegetation (HSV). Cropland, irrigated crops and rainfed crops fall under the cropland (CRP) category. Permanent river systems and the Allal El Fassi Reservoir are examples of water bodies (WTR). Road infrastructure, populated areas, and other human-made projects are examples of impermeable surfaces (IMP). Finally, the bare land, ice and snow (BAL) class includes high elevation areas that are covered with snow in season, as well as naturally exposed or artificial soils.

This classification system allows us to better capture the diversity of land surface conditions in the watershed than the general classification of land use and land cover. As the forest canopy is opened and degraded from lowland to highland, differentiating between dense and open forests, and the shrubland, herbaceous vegetation and bare ground, we can better show the land surfaces with different hydrological actions like rainfall interception, infiltration, surface runoff and soil protection. This classification system provides a good basis for the integrated use of land-use and land-cover data in hydrological models, water-erosion assessments, and reservoir sedimentation risk estimation. It is in line with local soil and water conservation needs. We use our sampling and validation strategy for the LULC_AllalEl-Fassi dataset to ensure that it is accurate, based on the features of the watershed, rather than external LULC products.

LULC change detection using the CCDC algorithm and Landsat time series

Land use and land cover changes can be classified into three different types. The first category is the regular changes that are representative of the natural cycle of plants. The second type is gradual changes that are due to prolonged human or natural processes such as slow growth or decline of vegetation. The third category is abrupt changes that are triggered by deforestation, wildfires, agricultural expansion, or urban development. A good monitoring of land use and land cover is to detect abrupt changes, but also to take into account regular seasonal fluctuations and slow long-term trends.

We visualize the spectral trajectories of individual pixels, and we identify the temporal breakpoints in this work with the CCDC algorithm. The technique is based on fitting satellite observations with a harmonic function that is a mixture of sinusoidal variables with periodic variations and trend variables.

$$\hat{\rho}(i,t) = a_{0,i} + c_{1,i} \times t + \Sigma_{k=1}^{n} \left(a_{k,i} \times cos\left(\frac{2k\pi}{T} \times t\right) + + b_{k,i} \times sin\left(\frac{2k\pi}{T} \times t\right) \right) \quad (1)$$

where: $\hat{\rho}(i,t)$ is the predicted surface reflectance of the i-th spectral band on Julian day t; $c_{1,i}$ et $a_{0,i}$ are the slope and intercept of the regression model for the i-th spectral band, respectively; $a_{k,i}$ et $b_{k,i}$ are the coefficients of the k-th harmonic component; n is the number of harmonic terms; and is the number of days in a year (typically 365).

After carefully balancing the advantages and limitations of higher-order harmonic terms, the number of harmonic components was ultimately set to (n = 3), following the recommendations of previous studies (Zhu and Woodcock, 2014b; Xian et al., 2022).

Since the continuous change detection (CCD) algorithm is a multivariate change detection technique that can be applied to a variety of land use and land cover types (Zhu, 2017b), three spectral indices (NDVI, NDWI, and NBR, Equations 2, 3 and 4) and five Landsat spectral bands – the blue band being excluded due to its sensitivity to atmospheric effects – were combined to identify the different kinds of changes found in the Landsat time series.

$$NDVI = \frac{(\rho\_nir - \rho\_r)}{(\rho\_nir + \rho\_r)} \quad (2)$$

$$NDWI = \frac{(\rho_{green} - \rho_{swir1})}{(\rho_{green} + \rho_{swir1})} \quad (3)$$

$$NBR = \frac{(\rho\_nir - \rho\_swir1}{(\rho\_nir + \rho\_swir1)} \quad (4)$$

where: ρ_green, ρ_r , ρ_nir, and ρ_swir1 indicate the green, red, near-infrared (*NIR*), and shortwave infrared 1 (*SWIR*1) bands' surface reflectance levels, respectively.

The least absolute shrinkage and selection operator (LASSO) algorithm was used to estimate the regression coefficients because it outperforms ordinary least squares regression by minimizing overfitting and efficiently managing irregularly distributed and occasionally sparse Landsat observations (Zhu and Woodcock, 2014).

The choice of the CCDC model's change-detection parameters affects its performance (Zhu and Woodcock, 2014; Zhu, 2017). Three crucial factors were taken into account: the minimal time span needed to stabilize the temporal model, the chi-square probability threshold utilized to find a breakpoint, and the lowest number of observations needed to fit a temporal segment. The temporal trajectories linked to the separate validation points were used in a sensitivity analysis. A minimum of five observations, a chi-square probability threshold of 0.95, and a minimum temporal period of two years were found to be the ideal parameter values based on this investigation (Table 1).

After fitting time series, we examined differences between observed and model-predicted reflectance values to detect land use and land cover change. We found that consecutive observations with differences exceeding the threshold of the algorithm were identified as breakpoints. Figure 3 shows two examples from the study area: (a) a spectral pattern that is stable over time and does not show a breakpoint, and (b) a spectral pattern that is abrupt.

Spatiotemporal consistency optimization

The monitoring of land use and land cover dynamics begins with the identification of altered pixels and their corresponding breakpoint dates. However, the assignment of new land use and land cover classes to each pixel following a detected change is not determined solely by change detection. To update land use and land cover data for affected areas, a locally adaptive classification process was implemented. This process is based on the creation of spatiotemporally stable training samples, extraction of topographic, textural, and spectral properties, classification of altered pixels, and optimization of the spatial and temporal consistency of the resulting maps.

The quality of training samples significantly influences the accuracy of land-use and land-cover mapping (Foody, 2010; Foody, 2011; Li et al., 2020; Huang et al., 2020). Although visual interpretation typically yields highly reliable training samples, it is time-consuming and challenging to apply across large areas and extended periods. In this study, extremely high-resolution imagery from Google Earth Pro was visually interpreted to collect 2000 training samples. The examination of spectral trajectories and Landsat false-color composites further supported the reliability of these samples. To ensure adequate representation of the geographical and spectral diversity of the eight land-use and land-cover classes, an automated sample selection process was applied to regions not covered by visual interpretation. Existing land-use and land-cover maps were superimposed on pixels identified by the CCDC algorithm as temporally stable between 1985 and 2025. A 3 × 3-pixel morphological erosion filter was used to refine the resulting overlap areas, eliminating boundary pixels and enhancing the spatial homogeneity of the training samples. These temporally stable regions were considered to provide a higher degree of certainty for sample creation. Although labeling errors may still occur in some automatically generated samples, previous research has demonstrated that the Random Forest classifier is robust to this type of label noise, provided that the proportion of incorrectly

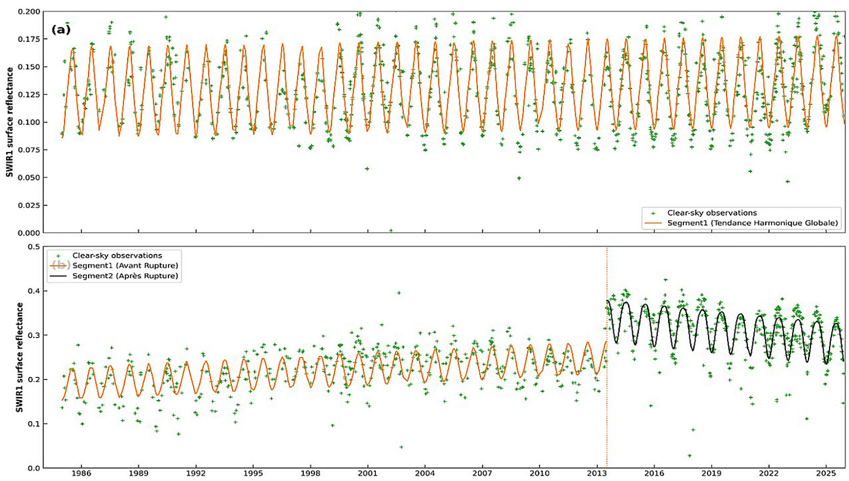

Figure 3. Two representative land use and land cover trajectories identified using the continuous change detection and classification (CCDC) algorithm and continuous Landsat observations: (a) a temporally stable condition with no detected breakpoint; (b) an abrupt land use and land cover change characterized by a breakpoint in the spectral trajectory

Table 1. Implementation parameters used for the CCDC and Random Forest models

Component	Parameter	Value
CCDC	Harmonic order	3
	Regression model	LASSO
	Spectral bands	Green, Red, NIR, SWIR1, SWIR2
	Spectral indices	NDVI, NDWI, NBR
	minObservations	5
	chiSquareProbability	0.95
	minNumOfYearScaler	2 years
Random Forest	Number of trees	500
	Variables per split	√p
	Training strategy	Stratified sampling
	Sample range	600–8000 samples/class
Optimization	Spatial window	3 × 3
	Temporal neighbourhood	Previous–Current–Next year
	Homogeneity threshold	0.50

identified samples remains below 20% (Mellor et al., 2015; Pelletier et al., 2017).

A sample approach proportionate to the area occupied by each land use and land cover class was used to lessen class imbalance. To prevent the underrepresentation of uncommon classes and the overdominance of the most common ones, a minimum of 600 and a maximum of 8.000 samples per class were selected. The Landsat time series was used to derive a set of predictive factors prior to model development. The NDVI, NDWI, and NBR spectral indices were combined with the 10th, 25th, 50th, 75th, and 90th percentiles of the five chosen optical bands to create multitemporal phenological features. These percentile composites lessen the impact of extreme values while capturing the seasonal variability of land use and land cover classifications.

For the 1985, 1990, and 1995 land use and land cover maps, a five-year temporal gap was chosen due to the scarcity of Landsat data before 2000, when Landsat 5 was the main source of satellite imagery. To improve the number of valid data available for analysis, observations obtained within a ±2-year temporal frame were used for each of these reference years. The improved accessibility of Landsat imagery starting in 2000 enabled the creation of annual land-use and land-cover maps through 2025.

The Random Forest algorithm was used to classify land use and land cover, as it has been proven to perform well in this context, despite noise and overfitting, and its high dimensional processing power (Breiman, 2001; Gislason et al., 2006; Belgiu and Drăguţ, 2016). 500 decision trees were used to develop the model using the Google Earth Engine platform. The square root of the total number of input variables was used to calculate the number of predictor variables that were evaluated at each split.

The predictor variables used for classification consisted of five Landsat spectral bands, three spectral indices (NDVI, NDWI, and NBR), multitemporal percentile compositions (10th, 25th, 50th, 75th, and 90th percentiles), GLCM textures based on the median NIR composite, and topographic parameters (elevation, slope, and aspect) based on ASTER GDEM. All Random Forest parameters are the default implementation of the Google Earth Engine smileRandomForest classifier to provide a consistent and reproducible classification approach.

Locally adaptive classification trains models from samples from the vicinity of altered pixels. As a result, the geographical, biological, and spectral characteristics of different watershed regions on the maps are captured more accurately with this method. During each mapping period, only pixels classified as changing by CCDC are reclassified, while stable pixels remain in their previous land-use and land-cover classifications. This way, we do not have to consider reclassifying the whole watershed for each period, and minimize artificial differences between maps.

Following the Random Forest classification, each of the 26 LULC maps was independently refined using a post-classification spatio-temporal optimization procedure designed to improve spatial coherence, reduce isolated classification errors, and enhance the overall temporal consistency of the reconstructed LULC series.

For each classified pixel we computed a homogeneity probability by considering both its spatial neighborhood (a moving window of 3 × 3) and its temporal neighborhood (the previous, current, and subsequent mapping dates). This probability quantifies the agreement between the class assigned to the central pixel and those of its spatial and temporal neighbors and is computed as follows:

$$P_{x,y,t} = \frac{1}{N}\Sigma_{x'=x-1}^{x+1}\Sigma_{y'=y-1}^{y+1}\Sigma_{t'=t-1}^{t+1}\cdot I\left(L_{x',y',t'} = L_{x,y,t}\right) \quad (5)$$

where: $P_{x,y,t}$ is the homogeneity probability of the pixel located at coordinates (x,y) at time (t); $L_{x,y,t}$ denotes the land use and land cover label assigned to the central pixel; $L_{x',y',t'}$ denotes the labels of the neighboring pixels; and I is an indicator function that takes the value **1** when the labels are identical and **0** otherwise; N is the total number of valid neighboring observations included in the calculation.

A probability threshold of 0.5 was used. Pixels with $P(x,y,t) \geq 0.5$ were considered sufficiently consistent and their original classification was retained. On the other hand, pixels with $P(x,y,t) < 0.5$ were regarded as uncertain and their class label was replaced by the majority class in the 3 × 3 spatial neighborhood as proposed by Chen et al. (2012) and Lv et al. (2018).This type of refinement was made only once for each mapping date and achieved a good reduction of isolated salt-and-pepper noise while preserving the spatial continuity of homogeneous land-cover patches, and also improving the temporal consistency of the reconstructed LULC series.

Accuracy assessment

The LULC_AllalElFassi dataset accuracy assessment was guided by good practice recommendations for land cover map validation by Olofsson et al. (2014). It consisted of two complementary measures: (i) the thematic accuracy assessment from an independent validation dataset for the benchmark year (2020) and (ii) the area-based assessment to assess the mapped extent of each land use and land cover class. (Olofsson et al., 2014).

For the benchmark year (2020), thematic classification accuracy was assessed using an independent confusion matrix derived from 800 stratified validation samples. This confusion matrix was used to calculate the producer's accuracy (PA), user's accuracy (UA), overall accuracy (OA), Cohen's Kappa coefficient, F1-score. Producer's Accuracy and User's Accuracy were calculated as follows:

$$P.A._k = \frac{p_{kk}}{\Sigma\, p_k} \quad (6)$$

$$U.A._k = \frac{p_{kk}}{\Sigma\, p_{.k}} \quad (7)$$

$$O.A = \Sigma_{k=1}^{m} p_{kk} \quad (8)$$

where: p_{kk} is the proportion of the mapped area classified as class (k) that is also assigned to class (k) in the reference dataset; $\Sigma\, pk$ and $\Sigma\, p.k$ denote the proportion of the mapped area classified as class (k) and the proportion of the reference area belonging to class (k), respectively; and (m) is the total number of land use and land cover classes.

To get a fair representation of the eight LULC classes, 800 independent validation samples were selected using a stratified random sampling strategy. The reference label for each validation point was obtained from using very high resolution imagery that is available in Google Earth Pro and where appropriate from Landsat time series and contextual information. None of the validation samples were used during classifier training to ensure independence between training and validation data.

For the historical mapping period (1985–2019) we did not have any reference data. Therefore, we evaluated the temporal quality of the dataset using the temporal consistency indicators (TCIs) rather than the overall accuracy metric. These indicators represent the temporal agreement among multiple complementary validation components rather than thematic classification accuracy derived from independent reference observations. Consequently, they provide an integrated measure of the temporal reliability and internal consistency of the reconstructed LULC series.

Finally, we measured the temporal performance of the LULC_AllalElFassi dataset by comparing the consistency of land-cover transitions through a binary change-detection task. For each of the mapping dates, we categorised the validation samples into two categories (changed and unchanged pixels) and generated a binary confusion matrix. To remove the effect of class imbalance between these two categories, we computed F1-score as:

$$F_1 = \frac{(P.A.\times\ U.A.)}{(P.A. + U.A.)} \times 2 \times 100\% \qquad (9)$$

The F1-score is the harmonic mean of the Producer's Accuracy and User's Accuracy and provides a balanced measure of change-detection performance that accounts for omission and commission errors.

The uncertainty of the Overall Accuracy and Cohen's Kappa coefficient was measured using a stratified non-parametric bootstrap. Roughly 1.000 bootstrap iterations were performed. During each bootstrap iteration we replaced the independent validation dataset with the reference LULC class in order to maintain the original sample set size. For each bootstrap sample we generated a confusion matrix and both the Overall Accuracy and Cohen's Kappa coefficient were calculated. The values after the (±) are the standard deviations of the bootstrap distributions. The 95% confidence intervals were estimated using percentile bootstrap method (2.5th and 97.5th percentile in the lower and upper confidence ranges respectively).

Temporal validation strategy

As a benchmark year (2020) we measured thematic classification accuracy with an independent validation dataset of 800 stratified reference data from Landsat time series and high resolution imagery. This benchmark year was the only time we could use independent data with which to compute standard accuracy parameters like OA, PA, UA, Cohen's Kappa coefficient and class-level F1-scores.

For the historical mapping (1985–2019) we did not have independent reference data, so it is hard to evaluate the historical maps accurately in the context of the thematic accuracy. Therefore we have used a temporal consistency indicator (TCI) to evaluate the temporal reliability of the reconstructed historical maps. Unlike the traditional overall accuracy, the TCI is not meant as a statistical measurement of classification accuracy but rather, as a temporal agreement score which sums the overall consistency amongst the complementary sources of evidence used in the historical validation process.

The TCI includes five complementary validation components: (i) visual interpretation of Landsat spectral trajectories, (ii) consistency of CCDC temporal breakpoints with the reconstructed land-cover trajectories, (iii) visual comparison with multi-temporal high resolution Google Earth imagery where available, (iv) comparison with existing regional and global LULC products, and (v) verification of unrealistic land-cover transitions through the post-classification spatio-temporal consistency optimization. Rather than relying on a single validation source, the TCI can provide a synthetic representation of the agreement of these complementary validation methods, and thus the overall temporal reliability of each reconstructed historical map.

Higher TCI values indicate better alignment between the different validation components and thus greater confidence in the temporal consistency of the reconstructed LULC maps. Lower values indicate higher uncertainty, mainly because of poor historical Landsat data during the early part of the time series. Therefore, the TCI should be considered as an indicator of the internal reliability and consistency of the reconstructed LULC series, not a thematic classification accuracy based on independent ground reference data.

Data and code availability

To ensure transparency and reproducibility, we have made all the resources developed in this study freely available in two sites. The LULC_AllalElFassi dataset (1985–2025), the Google Earth Engine scripts to preprocess the images, CCDC implementation, locally adaptive Random Forest classification and spatio-temporal consistency optimization, training and validation datasets, metadata and technical documentation and user guide can be easily found.

The full source code and workflow implementation are available in the public GitHub repository: https://github.com/mohamedBaaba/LULC_AllalElFassi. The dataset, documentation and related resources are also freely available through the SIG-Maroc geospatial platform at https://www.sig-maroc.com/donnees/lulc_AllalElFassi.

These public repositories provide immediate access to all materials needed to reproduce the methodology, reuse the dataset, and enable its application to other Mediterranean watersheds, in line with Open Science.

RESULTS AND DISCUSSIONS

Spatiotemporal overview of the LULC_AllalElFassi dataset and land use/land cover changes

An overview of the LULC_AllalElFassi dataset for 2025 is shown in Figure 4. The spatial distribution of the main land use and land cover classes within the Allal El Fassi watershed is generally accurately depicted in the generated map. The majority of the watershed is covered by the predominant land-cover class of herbaceous and sparse vegetation, especially in open landscapes and at mid elevations. Dense forests are mostly found in the Middle Atlas's hilly areas, where a continuous forest canopy is supported by good topography and climatic circumstances. The majority of open forests and shrublands are found in the areas that separate agricultural land from wooded areas. Alluvial plains, valleys, and regions with cultivable topography are the main locations for croplands. In contrast to the water bodies class, which is dominated by the Allal El Fassi Reservoir, whose impoundment has significantly altered the spatial structure of the terrain, impervious surfaces are still relatively small. They are mostly connected to urban areas, villages, and the main road network.

Significant spatial changes in the Allal El Fassi watershed are evident from the examination of land-use and land-cover dynamics between 1985 and 2025 (Figure 5). The most noticeable changes are concentrated in agricultural areas, transitional zones between forest ecosystems and open landscapes, and along the reservoir's edges, according to the change intensity map (Figure 5a), which is derived from the percentage of altered pixels within 500 m grid cells. Three main processes characterize these modifications. The first is the gradual growth of agricultural land, which mostly happens at the expense of native plants. The second is related to the spatial oscillations of wetlands and water bodies, which are directly influenced by changes in reservoir water levels. This phenomenon has been extensively studied globally (Patel et al., 2015). The third is herbaceous and sparse vegetation, which is sensitive to climate changes, especially in Mediterranean and semi-arid regions, as evidenced by its significant geographical variability (Petrosillo et al., 2021).

Figure 5b shows the quantitative changes in the eight land use and land cover classifications. The findings indicate that impermeable surfaces increased by 789.63% (+664 ha), and open forests increased by 898.50% (+2.704 ha). Dense forests, on the other hand, declined by 9.35% (−2.996 hectares), indicating a slow change in the structure of the forest canopy. While herbaceous and scant vegetation decreased by 4.73% (−12,838 hectares), croplands increased by

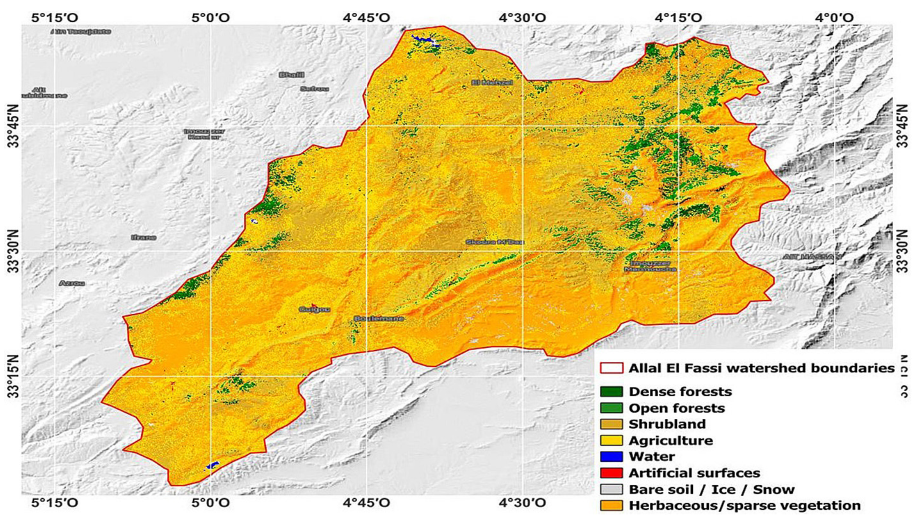

Figure 4. Overview of the LULC_AllalElFassi dataset for the year 2025. The classification scheme and color palette are adapted from the ESA Climate Change Initiative (ESA-CCI) Land Cover classification system

10.38% (+12,346 ha). In comparison to the other land use and land cover classifications, changes in shrublands (−0.10%), water bodies (−0.96%), and bare land, ice, and snow (+0.17%) remained comparatively small. Overall, these findings show that three processes that have significantly altered the watershed's spatial organization − the gradual opening of forest ecosystems, the increase of urbanized regions, and the expansion of agricultural land − dominate landscape dynamics.

Transitions between land-use and land-cover classes were examined using a Sankey diagram (Figure 6) to identify the primary landscape-modification trajectories. The findings show that a significant portion of the watershed remained constant over the course of the study, particularly in the main land-use and land-cover classifications. However, several noteworthy shifts are discernible. The main source class for land cover conversions is herbaceous and sparse vegetation, and over the previous forty years, a sizable amount of this class has been converted into croplands. Although a portion of their territory changed to open forests and shrublands, indicating a gradual decrease in forest canopy density, dense forests generally showed excellent spatial stability. The primary populated sections of the watershed continued to be urbanized, as seen by the increase of impervious surfaces, which remained relatively small in absolute area but mostly at the expense of croplands and, to a lesser extent, herbaceous and sparse vegetation.

Three example sectors were chosen to better highlight the key land-use and land-cover processes observed (Figure 7). The first focuses on the agricultural expansion front near Ribat El Kheir, where croplands have gradually replaced herbaceous and sparse vegetation since the 1990s, increasing the fragmentation of natural environments. The second example shows how impermeable surfaces have steadily increased over the past forty years in the urban areas of El Menzel and Ribat El Kheir, as well as in the neighboring rural villages (douars). Lastly, the Allal El Fassi Reservoir is represented by the third sector, which shows how well the LULC_AllalElFassi dataset captures shoreline variations. The findings show that, in response to variations in reservoir water levels, there are alternating water bodies and barren land classes, as well as a progressive increase in impermeable surfaces along the reservoir edges.

The LULC_AllalElFassi dataset reliably captures the main spatiotemporal dynamics that occurred within the watershed between 1985 and 2025, based on a combined analysis of land-use and land-cover maps, change trajectories, and representative local subsets. For long-term monitoring of land use and land cover change at the

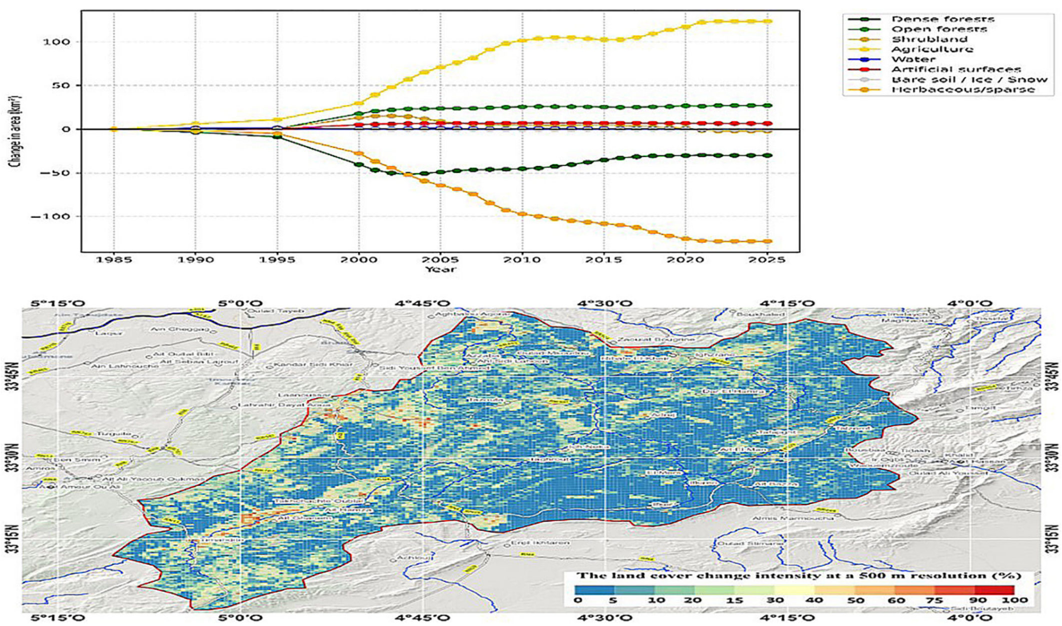

Figure 5. Land use and land cover dynamics in the Allal El Fassi watershed from 1985 to 2025: (a) spatial change intensity calculated at a 500 m spatial resolution; (b) cumulative changes in the area of the eight land use and land cover classes

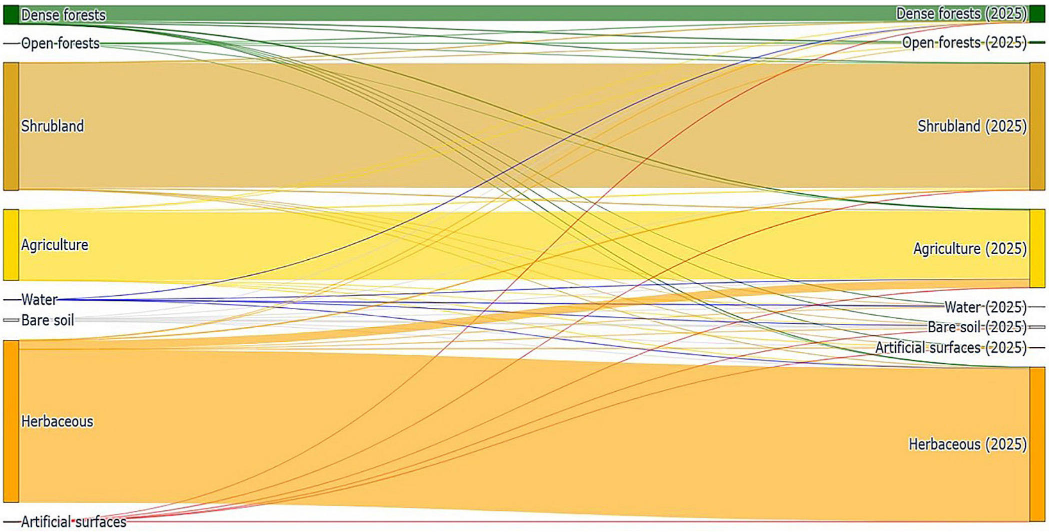

Figure 6. Sankey diagram illustrating the major land-use and land-cover transitions in the Allal El Fassi watershed between 1985 and 2025

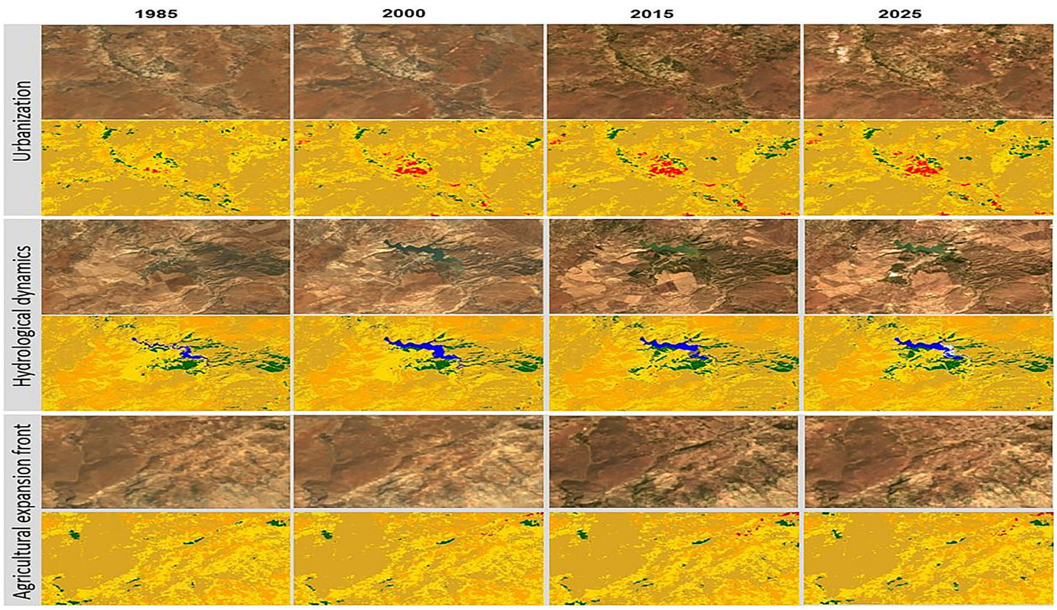

Figure 7. Three representative close-up views illustrating land use and land cover changes derived from the LULC_AllalElFassi dataset between 1985 and 2025: (a) the agricultural expansion front around Ribat El Kheir; (b) urbanization in the vicinity of El Menzel and Ribat El Kheir; and (c) the hydrological dynamics of the Allal El Fassi Reservoir

watershed scale, the quality of the data validates the efficacy of integrating Landsat time series with the CCDC method.

Accuracy assessment of the LULC_AllalElFassi classification

We have evaluated LULC_AllalElFassi classification performance on an independent dataset for the benchmark year 2020. The confusion matrix (Table 2) gives an OA of 82.82% and Cohen's Kappa of 0.8012. The bootstrap standard deviations are 0.45 percentage points for the OA and 0.0062 for Cohen's Kappa, indicating that the classified map is very well matched to the independent dataset. In addition to the overall accuracy, PA, UA, and class-level F1-scores were calculated for each land use and land cover class to further assess the classification performance. These metrics measure omission and commission errors for each class, and provide an insight into the reliability and robustness of our classification framework.

Croplands, impervious surfaces, and water bodies have the highest accuracy level. For water bodies, user accuracy was 94.94% and producer accuracy was 93.65%, respectively. The high precision is mainly due to the water spectral signature in the near-infrared and shortwave infrared bands, which is very strong in water absorption. Impervious surfaces have a producer's accuracy of 92.65% and a user's accuracy of 95.51%. Most of the class errors in this class result from croplands and barren land, particularly in peri-urban areas where multiple land-cover types are present within a single pixel. Croplands also performed well, with producers' accuracy of 87.64% and users' accuracy of 86.71%. Most of the class errors involve herbaceous and sparse vegetation and shrublands, especially in fallow fields, abandoned farmland, and areas where cultivated land and natural vegetation are separated. Forests also had good classification results with producer accuracy of 87.81% and user accuracy of 89.55%. These results emphasize the importance of spectral, textural, and topographic information for classification and underscore the need to use the canopy cover threshold to separate dense forests from other tree types. Open forests showed a moderate classification performance with producer accuracy of 72.34% and user accuracy of 74.28%. Most of the misclassifications of open forests occurred in dense forests, shrubland, and, to a lesser extent, herbaceous and sparse vegetation, due to the slow evolution of canopy density in these vegetation types.

Shrublands (SHR) and herbaceous and sparse vegetation (HSV) had the lowest classification accuracy. For SHR, the producer's accuracy is 58.64%, and the user's accuracy is 62.80%. For HSV, the producer's accuracy is 61.18%, and the user's accuracy is 72.10%. The lower accuracies are related mainly to the diversity and spatial distribution of vegetation types. In transitional regions of the watershed, shrublands, dry herbaceous vegetation, and bare land often co-occur and have similar spectral signatures, especially during periods of water shortage or low vegetation activity. This is the reason for the confusion between the SHR, HSV, and BAL classes in the confusion matrix.

We also closely examine the confusion matrix and identify typical misclassification patterns in semi-arid and Mediterranean areas. The presence of deep forest understory, forest clearings, and 30 m spatial resolution, which increases the number of mixed pixels, probably contributes to the 3.21% misclassification rate between dense forests and herbaceous and sparse vegetation. 13.91% of BAL pixels were classified as HSV, indicating substantial misclassification between bare ground and herbaceous and sparse vegetation. However, 9.94% of HSV pixels were classified as BAL. This shows that when there is water stress, the open soil areas can be hard to distinguish between the herbaceous and dry land, and the herbaceous areas

Table 2. Confusion matrix and accuracy of the LULC_AllalElFassi dataset in 2020. The abbreviations refer to the eight land-use and land-cover classes

Classe	DF	OF	SHR	HSV	CRP	WTR	IMP	BAL	Total	U.A (%)	F1
DF	87 .81	2.15	4.52	3.21	0.85	0.00	0.21	1.25	100	89.55	88.67
OF	8.42	72.34	10.15	5.68	1.24	0.00	0.00	2.17	100	74.28	73.30
SHR	1.24	3.87	58.64	18.42	4.21	0.00	0.00	13.62	100	62.80	60.65
HSV	2.18	2.45	15.83	61.18	8.42	0.00	0.00	9.94	100	72.10	66.19
CRP	0.84	0.62	3.88	5.55	87.64	0.00	0.84	0.63	100	86.71	87.17
WTR	0.00	0.00	0.00	0.00	0.00	93.95	0.00	6.35	100	94.94	94.29
IMP	0.00	0.00	0.00	0.00	2.84	0.00	92.65	4.51	100	95.51	94.06
BAL	0.84	1.25	5.62	13.91	1.24	0.00	1.24	75.90	100	78.22	77.04
Total	100	100	100	100	100	100	100	100	-----	----	
P.A. (%)	87.81	72.34	58.64	61.18	87.64	93.65	92.65	75.90	O.A = 82.82 ±0.45 percentage points		
Cohen's Kappa									Kappa = 0.80 ±0.0062		

Note: N.B: The values following (±) represent the standard deviations obtained from 1.000 stratified bootstrap resamples. The corresponding 95% confidence intervals were estimated using the 2.5th and 97.5th percentiles of the bootstrap distributions.

that have been vegetated in the open. The fallow fields, harvested croplands, or agricultural land temporarily recolonized by spontaneous vegetation are likely responsible for the 5.55% confusion between croplands and herbaceous and sparse vegetation. The difference between shrubland and herbaceous and sparse vegetation was particularly pronounced: 18.42% of SHR pixels were classified as HSV, and 15.83% of HSV pixels were classified as SHR, and the challenge is to distinguish between two communities with similar vegetation structure and spectral structure.

The next statistical indicators also demonstrate the robustness of the classification framework. The Cohen's Kappa coefficient shows a strong agreement beyond chance and the class-level F1-scores for most land use and land cover classes are close to the producer's and user's accuracies. Lower F1-scores for shrubland and herbaceous and sparse vegetation are consistent with the ecological continuity and spectral similarity of the Mediterranean vegetation formations which are still one of the main sources of classification uncertainty.

The LULC_AllalElFassi dataset has a total accuracy of 82.82% in comparison to other recent high resolution land use and land cover products, such as GLC_FCS30 (82.50%) and CLCD (81.52%). Our dataset also outperforms some of the global products widely used, such as GlobeLand30 (79.30%), FROM_GLC (76.20%), MCD12Q1 (73.60%) and ESA CCI-LC (71.50%). While comparing our dataset and other products shows that our product does well in classification, we should be careful from here on because the data we have included in our dataset do not have the same classification system, validation methodologies, spatial coverage, and applications.

In addition to the Overall accuracy, Table 3 shows that there are key differences between the datasets. While products like GLC_FCS30 and CLCD have high classification accuracy and partial or complete class-level validation, LULC_AllalElFassi has a competitive overall performance alongside a comprehensive class-specific accuracy assessment with PA, UA and F1-score for all land cover classes. Furthermore, the dataset has a spatial consistency optimization to reduce the isolated classification noise and increase the spatial coherence of the final maps. Unlike global and continental products based on general classification procedures, LULC_AllalElFassi was developed for the Allal El Fassi watershed using the locally adapted classification system to better simulate Mediterranean vegetation and the hydrological landscape. This method allows us to provide a more realistic portrayal of the land-cover dynamics in the area while still using the 30-m spatial resolution of Landsat-based products.

The temporal consistency data indicated that LULC_AllalElFassi also showed a good internal consistency over the course of the study. The mean temporal consistency was 79.66%, with a maximum of 80.05% in 2015 and a minimum of 78.90% in 2000. In contrast to the thematic overall accuracy for the benchmark year (2020), these numbers do not represent classification accuracy based on individual historical reference. They provide a summary of the internal consistency of the time series generated based on the complementary temporal validation framework, including the interpretation of Landsat time series, the trajectory analysis of CCDC, the viewing of high-resolution images, the comparison with existing LULC products, and the post-classification consistency analysis (Roy et al. 2014).

Table 3. Comparison of the Overall accuracy of the LULC_AllalElFassi dataset with some existing land use and land cover products

Produit	R	O.A (%)	Kappa	PA/UA/F1	Spatial consistency	References
LULC_AllalELFassi	30 m	82.82	0.80	Yes (all classes)	Yes	Our Study
GLC_FCS30	30 m	82.5	0.784	Partial	Yes	(Zhang et al., 2021)
CLCD	30 m	81.52	--	Yes (PA, UA and F1 by class)	Yes	(Yang and Huang, 2021)
ESA CCI_LC	30 m	71.5	--	Partial	Limited	Defourny et al. (2018)
MCD12Q1	30 m	73.6	--	Partial	Limited	Sulla-Menashe et al. (2019)
FROM_GLC	30 m	76.2	--	Partial	Moderate	(Gong et al., 2013)
GlobelLand30	30 m	79.3	--	Partial	Moderate	(Chen et al., 2015)

These results are consistent with the temporal validation strategy. While we could only provide reference data for the benchmark year (2020), we also evaluated historical maps using a similar consistency-based approach that includes visualisation of Landsat time series, high-resolution Google Earth images, CCDC temporal trajectories, and comparisons with existing land cover products. The small interannual variation in temporal consistency indicator also supports the temporal stability and internal consistency of the LULC_AllalElFassi dataset during the 1985–2025 period.

Still, the temporal validation of the historical maps (1985–2019) is indirect and based on historical ground reference data rather than a direct measurement of temporal consistency indicator. Therefore, we should view the temporal accuracies as a sign of internal consistency and reliability of the produced time series rather than a measure of temporal consistency indicator. While Landsat time-series interpretation, CCDC trajectory analysis, high-resolution imagery, and comparisons with existing land cover products all provide a strong complementary tool for the assessment of long-term land use and land cover over the first years of the Landsat archive, uncertainty still remains (Figure 8).

There was a marked difference between producers' accuracy (PA) and users' accuracy (UA) over time for different land use and land cover types. Croplands, water bodies, and impermeable surfaces all exhibited very good and stable accuracy due to their distinct spectral characteristics and well-defined spatial distributions. In contrast, shrublands, herbaceous vegetation, and sparse vegetation had more erratic accuracy during drought years. The fluctuations were due to reduced photosynthetic activity, more soil exposure, and the spectral similarity of herbaceous vegetation, shrublands, and bare land, which complicated classification (Figure 9).

The class areas predicted from the map and those generated from the reference data likewise show good agreement, according to the area bias evaluation. The best classification performance was confirmed by the lowest area biases, both of which were less than 1% for water bodies and impermeable surfaces. The mapped extent of dense woods was slightly overestimated, as seen by their positive area bias of +2.5%. With values of −4.2% and +3.8%, respectively, shrublands and herbaceous and sparse vegetation showed the biggest biases. These differences indicate a propensity to overestimate herbaceous vegetation while underestimating shrubland areas, which aligns with the confusion matrix's misclassification tendencies between these two classes (Figure 10).

Analysis of land use/land cover changes from 1985 to 2025

The areas occupied by the eight land-use and land-cover groups in 1985 and 2025, along with their relative changes and mean annual rates of change, are summarized in Table 4. Over the 40-year study period, the Allal El Fassi watershed exhibited varied land-use and land-cover patterns. While shrublands, water bodies, bare ground, ice, and snow showed relatively little change, the most noticeable changes are linked to the gradual opening of the forest canopy, the rise of impermeable surfaces, and the expansion of croplands.

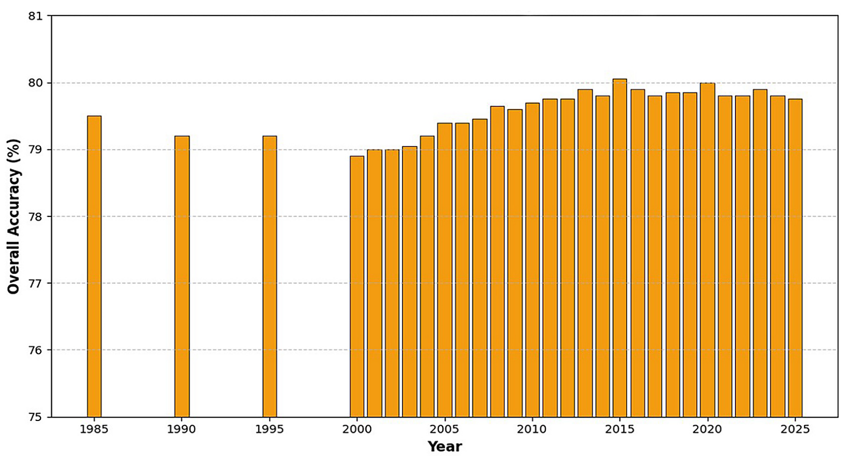

Figure 8. Temporal consistency indicators (TCIs) for the historical LULC maps (1985–2019)

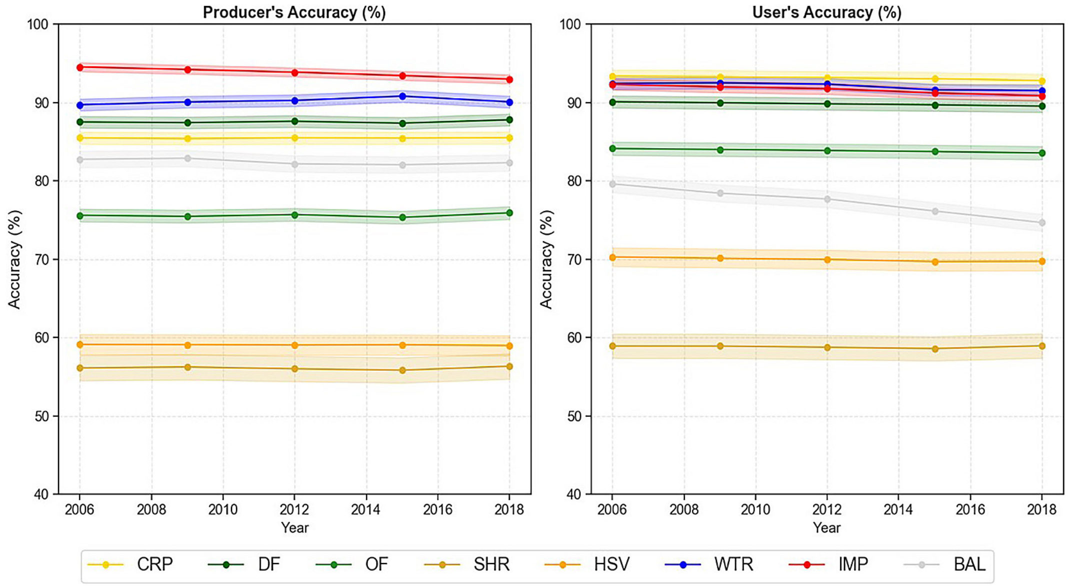

Figure 9. Temporal evolution of producer's accuracy (PA) and user's accuracy (UA) for the eight land use and land cover classes of the LULC_AllalElFassi dataset from 1985 to 2025

During the research period, one of the most notable changes to the landscape was the alteration in forest cover. Between 1985 and 2025, the area of dense forests decreased from 32,072 ha to 29,076 ha. This represents a loss of 2.996 ha, a relative decrease of 9.35%, and a mean annual rate of change of −0.25%. Open forests grew from 301 ha to 3.005 ha during that time, a gain of 2,704 ha, a relative growth of 898.50%, and a mean annual rate of change of 5.92%. The strong correlation between the increase in open forests and the decrease in thick forests indicates that a significant portion of this change was driven by an internal shift in forest cover. The gradual opening of forest stands, driven by the combined effects of fuelwood exploitation, wildfires, forest fragmentation, livestock grazing, selective logging, and water stress, is probably reflected in this shift. The remarkably large relative rise in open forests, however, should be viewed with caution because the percentage shift is mechanically amplified by their extremely small initial extent in 1985.

Over the course of the study, croplands significantly expanded. Between 1985 and 2025, their area grew from 118,960 ha to 131,306 ha, a gain of 12,346 ha, a relative increase of 10.38%, and

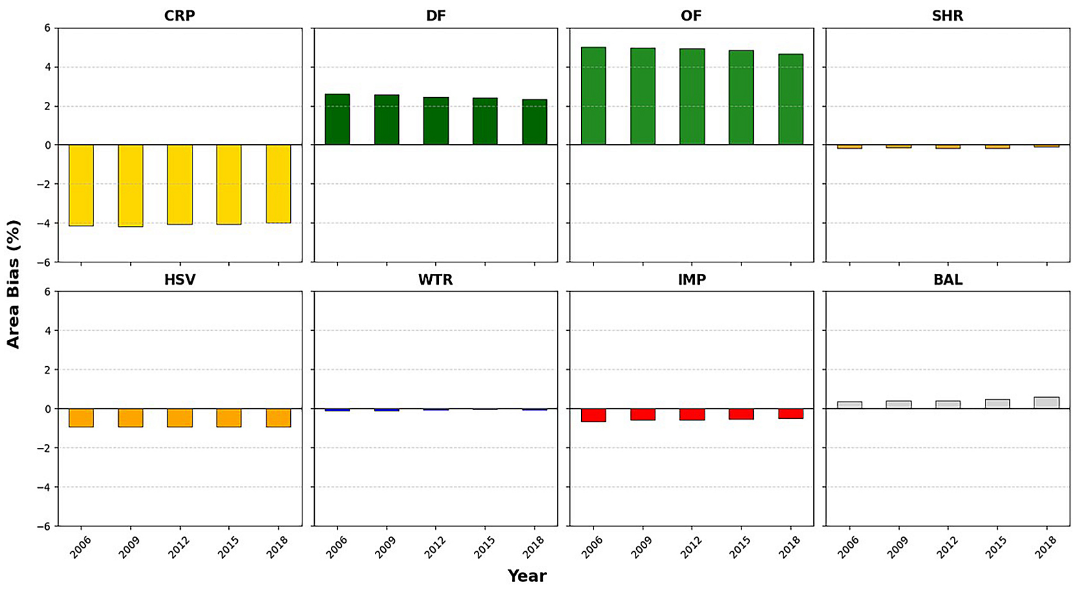

Figure 10. Estimated area bias for the eight land use and land cover classes of the LULC_AllalElFassi dataset

Table 4. Area and rates of change of the land use and land cover classes in the Allal El Fassi watershed between 1985 and 2025

Class	1985 (ha)	2025 (ha)	Change (%)	Annual rate (%)
Dense forests (DF)	32 072	29 076	−9.35	−0.25
Open forests (OF)	301	3 005	+898.50	+5.92
Shrubland (SHR)	214 030	213 822	−0.10	−0.002
Croplands (CRP)	118 960	131 306	+10.38	+0.25
Water bodies (WTR)	468	463	−0.96	−0.02
Built-up areas (IMP)	84	748	+789.63	+5.62
Bare land, ice and snow (BAL)	4132	4 139	+0.17	+0.004
Herbaceous and sparse vegetation (HSV)	271677	258 839	−4.73	−0.12

a mean annual rate of growth of 0.25%. This pattern suggests that one of the main forces behind the watershed's changing topography has been agricultural growth. At the expense of herbaceous and sparse vegetation, the spread of cultivated land most likely occurred in regions with favorable topography, particularly valleys, plateaus, and open landscapes. This pattern shows the intensification of agricultural land use and rising strain on natural vegetation.

During the study period, shrublands were almost unchanged worldwide, with an overall decrease of only 208 hectares, from 214,030 hectares in 1985 to 213,822 hectares in 2025. This loss of 208 hectares represents a 0.10 percent decrease and an average annual change in shrubland cover of -0.002%. The entire watershed changes, and the differences between shrublands, open woodlands, herbaceous and sparse vegetation, and croplands would be balanced. So even if shrublands are always relatively stable, there are still local changes in land cover. In contrast, herbaceous and sparse vegetation declined more drastically from 271,677 hectares (in 1985) to 258,839 hectares (in 2025). This is a total loss of 12,838 hectares with an average annual decrease of -0.12% and a relative decline of 4.73%. Most of this reduction is due to the conversion of herbaceous areas to cropland. In some areas, there are also connections to such areas becoming shrublands or open forests due to the return of natural vegetation, changes in grazing practices, or ecological restoration projects.

The area of water bodies decreased from 468 ha in 1985 to 463 ha in 2025, representing a loss of 5 ha, a relative reduction of 0.96%, and a mean annual rate of change of −0.02%. Over the course of the study, there was only a slight net change. The significant interannual variations in the water level of the Allal El Fassi Reservoir should not be obscured by this apparent constancy between the two reference years. When precipitation, hydrological inflows, droughts, water withdrawals, and reservoir management techniques occur, the reservoir's surface area may change significantly. Therefore, rather than consistent hydrological stability over the study period, the slight variation between 1985 and 2025 is mostly due to the similarity of the mapped water extent between these two years.

During the study period, impervious surfaces showed one of the highest relative rates of increase. Between 1985 and 2025, their area grew from 84 ha to 748 ha, a gain of 664 ha, a relative increase of 789.63%, and a mean annual rate of change of 5.62%. This trend reflects the watershed's rapid urbanization and infrastructure development, even though its overall extent remains smaller than that of the predominant agricultural and natural land cover classes. Therefore, land artificialization and the fragmentation of natural and agricultural landscapes have increased due to the growth of urban centers, rural villages (douars), the road network, and related infrastructure.

The total area of bare land, ice, and snow increased slightly from 4.132 ha in 1985 to 4.139 ha in 2025 (7 ha), or a relative increase in percentage of 0.17%, but the average annual rate of change was 0.004%. Overall, this category remained almost unchanged in the entire study. The total extent of exposed surfaces is relatively constant between the two reference years, as indicated by the relatively small net change. However, localized gains and losses can be offset by watershed changes, and bare land could be subject to significant seasonal and interannual variation due to drought, snow cover at higher elevations, and agriculture.

While the proposed framework performed well, it must still be acknowledged when interpreting the long-term land use and land cover trends. The main limitation is the lack of consistent historical ground reference data for the early years of the Landsat archive and therefore the use of traditional thematic validation prior to 2020. As a result, we have evaluated the reliability of the historical maps using a complementary temporal consistency strategy that uses visual interpretation of the Landsat time series, high-resolution Google Earth images, CCDC temporal trajectories, and comparisons with regional and global land cover products. This approach is not entirely sufficient to replace the historical field observations, but it does demonstrate the internal consistency of the generated data over the whole period of 1985–2025. When the historical reference data and the high-resolution satellite observations, such as Sentinel-1 and Sentinel-2 images, are combined we will be able to better validate the temporal accuracy and thematic accuracy of the long-term LULC products.

CONCLUSIONS

Our work developed LULC_AllalElFassi, the first 30 m spatio-temporal land use and land cover dataset for the Allal El Fassi Watershed from 1985 to 2025. Instead of introducing a new change detection algorithm, our work combined the existing CCDC approach with spatio-temporally stable sample generation, locally adaptive classification, and spatio-temporal consistency to obtain a consistent LULC time series. The dataset has an overall accuracy of 82.82 percentage points, which is good enough to show the robustness of our proposed mapping dataset. The generated maps show that over the past four decades the landscape has changed dramatically: forests have been opened further, croplands have expanded, and the impervious surface has grown fast– indicating the increasing pressure of humans on the watershed. However, we need to be mindful that our dataset is limited in terms of the 30 m Landsat spatial resolution, pixel density, historical image availability, and spectral similarity between the transition vegetation classes.

In addition to its research contribution, LULC_AllalElFassi also provides an operational dataset for environmental monitoring, hydrological modelling, water erosion assessment, reservoir sedimentation studies, forest management, and land-use planning. As a way to ensure that the data is fully transparent and reproducible, the full dataset, Google Earth Engine scripts, training/validation samples, workflow documentation, and metadata will be made available on SIG-Maroc and GitHub. Future work will also make use of Sentinel-2 optical imagery and Sentinel-1 radar observations to better distinguish the different kinds of vegetation and improve the spatial and temporal accuracy of the dataset. In general, our framework can be easily applied in other Mediterranean watersheds that face similar issues of land use and land cover change, climate change, and sustainable management of natural resources.

REFERENCES

1. Amarty FE, Chakir A, Benaabidate L, Lahrach A. (2025). Assessing landslide susceptibility using analytical hierarchy process (AHP) and frequency ratio (FR) in the Oued Lebene Watershed, North Morocco. *Iraqi Journal of Science*, 3981–4000. https://doi.org/10.24996/ijs.2025.66.9.36
2. Andreu V, Rubio JL, Gimeno-García E, Llinares JV. (1998). Testing three Mediterranean shrub species in runoff reduction and sediment transport. *Soil and Tillage Research. 45*(3), 441–454. https://doi.org/10.1016/S0933-3630(97)00040-8
3. Bai R, Yan W, Xiao Y, Wang S, Tian X, Li J, Xiao X, Lu X, Zhao F. (2020). Acceleration of peroxymonosulfate decomposition by a magnetic $MoS_2/CuFe_2O_4$ heterogeneous catalyst for rapid degradation of fluoxetine. *Chemical Engineering Journal. 397*, 125501. https://doi.org/10.1016/j.cej.2020.125501
4. Belgiu M, Drăguţ L. (2016). Random forest in remote sensing: A review of applications and future directions. *ISPRS Journal of Photogrammetry and Remote Sensing. 114*, 24–31. https://doi.org/10.1016/j.isprsjprs.2016.01.011
5. Bellin N, van Wesemael B, Meerkerk A, Vanacker V, Barbera GG. (2009). Abandonment of soil and water conservation structures in Mediterranean ecosystems: A case study from south east Spain. *CATENA. 76*(2), 114–121. https://doi.org/10.1016/j.catena.2008.10.002
6. Bengtsson J, Bullock JM, Egoh B, Everson C, Everson T, O'Connor T, O'Farrell PJ, Smith HG, Lindborg R. (2019). Grasslands – more important for ecosystem services than you might think. *Ecosphere. 10*(2), e02582. https://doi.org/10.1002/ecs2.2582
7. Boellstorff D, Benito G. (2005). Impacts of set-aside policy on the risk of soil erosion in central Spain. *Agriculture, Ecosystems & Environment. 107*(2), 231–243. https://doi.org/10.1016/j.agee.2004.11.002
8. Borrelli P, Robinson DA, Panagos P, Lugato E, Yang JE, Alewell C, Wuepper D, Montanarella L, Ballabio C. (2020). Land use and climate change impacts on global soil erosion by water (2015–2070). *Proceedings of the*

National Academy of Sciences. 117(36), 21994–22001. https://doi.org/10.1073/pnas.2001403117

9. Breiman L. (2001). Random Forests. *Machine Learning. 45*(1), 5–32. https://doi.org/10.1023/A:1010933404324
10. Cammeraat LH, Imeson AC. (1999). The evolution and significance of soil–vegetation patterns following land abandonment and fire in Spain. *CATENA. 37*(1), 107–127. https://doi.org/10.1016/S0341-8162(98)00072-1
11. Cerdan O, Govers G, Le Bissonnais Y, Van Oost K, Poesen J, Saby N, Gobin A, Vacca A, Quinton J, Auerswald K, et al. (2010). Rates and spatial variations of soil erosion in Europe: A study based on erosion plot data. *Geomorphology. 122*(1), 167–177. https://doi.org/10.1016/j.geomorph.2010.06.011
12. Chen Jun, Chen Jin, Liao A, Cao X, Chen L, Chen X, He C, Han G, Peng S, Lu M, et al. (2015). Global land cover mapping at 30 m resolution: A POK-based operational approach. *ISPRS Journal of Photogrammetry and Remote Sensing. 103*, 7–27. https://doi.org/10.1016/j.isprsjprs.2014.09.002
13. Chen X, Chen J, Shi Y, Yamaguchi Y. (2012). An automated approach for updating land cover maps based on integrated change detection and classification methods. *ISPRS Journal of Photogrammetry and Remote Sensing. 71*, 86–95. https://doi.org/10.1016/j.isprsjprs.2012.05.006
14. Claverie M, Ju J, Masek JG, Dungan JL, Vermote EF, Roger J-C, Skakun SV, Justice C. (2018). The harmonized Landsat and Sentinel-2 surface reflectance data set. *Remote Sensing of Environment. 219*, 145–161. https://doi.org/10.1016/j.rse.2018.09.002
15. Cosandey C, Andréassian V, Martin C, Didon-Lescot JF, Lavabre J, Folton N, Mathys N, Richard D. (2005). The hydrological impact of the mediterranean forest: a review of French research. *Journal of Hydrology. 301*(1), 235–249. https://doi.org/10.1016/j.jhydrol.2004.06.040
16. El Amarty F, Chakir A, Hattafi Y, Fikri N, Benaabidate L, Abderrahim L. (2024). Qualitative evaluation and mapping of water erosion risks in the Central Pre-Rif (Northern Morocco) – the case of the Oued Lebene Watershed. *Ecol Eng Environ Technol. 25*(12), 253–268. https://doi.org/10.12912/27197050/193867
17. El Amarty F, Chakir A, Purohit S, Elhag M, Lakhili F, Benaabidate L, Lahrach A. (2025). Comparative evaluation of machine learning models and remote sensing data for wildfire prediction in the Atlas Middle Forest, Morocco. *Earth Syst Environ* [Internet]. [accessed 2026 Jan 2]. https://doi.org/10.1007/s41748-025-00823-8
18. El Amarty F, Lahrach A, Benaabidate L, Chakir A. (2024). Estimating soil erosion and sediment yield using geographic information system in the Central Pre-Rif (Northern Morocco) – the case of the Oued Lebene Watershed. *Ecol Eng Environ Technol. 25*(8), 1–16. https://doi.org/10.12912/27197050/187977
19. Fikri N, Hattafi Y, Amartey FE, Lakhili F, Benaabidate L, Lahrach A. (2026). Application of locally produced biochar to mitigate soil erosion in the Oued Leben catchment, Fez–Meknes Region, Morocco. *Euro-Mediterr J Environ Integr. 11*(5), 159. https://doi.org/10.1007/s41207-026-01127-7
20. Foody GM. (2010). Assessing the accuracy of land cover change with imperfect ground reference data. *Remote Sensing of Environment. 114*(10), 2271–2285. https://doi.org/10.1016/j.rse.2010.05.003
21. Foody GM. (2011). Impacts of imperfect reference data on the apparent accuracy of species presence–absence models and their predictions. *Global Ecology and Biogeography. 20*(3), 498–508. https://doi.org/10.1111/j.1466-8238.2010.00605.x
22. García-Ruiz JM, Beguería S, Lana-Renault N, Nadal-Romero E, Cerdà A. (2017). Ongoing and emerging questions in water erosion studies. *Land Degradation & Development. 28*(1), 5–21. https://doi.org/10.1002/ldr.2641
23. Gislason PO, Benediktsson JA, Sveinsson JR. (2006). Random Forests for land cover classification. *Pattern Recognition Letters. 27*(4), 294–300. https://doi.org/10.1016/j.patrec.2005.08.011
24. Gong P, Wang J, Yu Le, Zhao Yongchao, Zhao Yuanyuan, Liang L, Niu Z, Huang X, Fu H, Liu S, et al. (2013). Finer resolution observation and monitoring of global land cover: first mapping results with Landsat TM and ETM+ data. *International Journal of Remote Sensing. 34*(7), 2607–2654. https://doi.org/10.1080/01431161.2012.748992
25. Gorelick N, Hancher M, Dixon M, Ilyushchenko S, Thau D, Moore R. (2017). Google Earth Engine: Planetary-scale geospatial analysis for everyone. *Remote Sensing of Environment. 202*, 18–27. https://doi.org/10.1016/j.rse.2017.06.031
26. Hasnae A, Hattafi Y, Amarty FE, Abderrahim L. (2026). Modeling and assessment of water erosion in the Aggay Watershed: A Machine Learning-based approach. *International Journal of Ecosystems and Ecology Science (IJEES) 16*(1), 353–566.
27. Hattafi Y, Amarty FE, Abderrahim L. (2026). Integrated gis-based evaluation of soil loss and sediment yield in the Audour Catchment, Northwestern Morocco. *International Journal of Ecosystems and Ecology Science (IJEES) 16*(1), 379–388.
28. Huang H, Wang J, Liu C, Liang L, Li C, Gong P. (2020). The migration of training samples towards dynamic global land cover mapping. *ISPRS Journal of Photogrammetry and Remote Sensing. 161*, 27–36. https://doi.org/10.1016/j.isprsjprs.2020.01.010
29. Lakhili F, Amarty FE, Chakir A, Hattafi Y, Fikri N, Benaabidate L, Lahrach A. *Comparative evaluation of machine learning model and PAP/CAR approach for water erosion prediction in the Beht watershed, Morocco* [Internet]. [accessed 2026 July 22]. https://

www.ecoeet.com/Comparative-evaluation-of-machine-learning-model-and-PAP-CAR-approach-for-water-erosion,203663,0,2.html

30. Li W, Dong R, Fu H, Wang J, Yu L, Gong P. (2020). Integrating Google Earth imagery with Landsat data to improve 30-m resolution land cover mapping. *Remote Sensing of Environment. 237*, 111563. https://doi.org/10.1016/j.rse.2019.111563
31. Lv Z, Liu T, Zhang P, Atli Benediktsson J, Chen Y. (2018). Land cover change detection based on adaptive contextual information using bi-temporal remote sensing images. *Remote Sensing. 10*(6), 901. https://doi.org/10.3390/rs10060901
32. Mellor A, Boukir S, Haywood A, Jones S. (2015). Exploring issues of training data imbalance and mislabelling on random forest performance for large area land cover classification using the ensemble margin. *ISPRS Journal of Photogrammetry and Remote Sensing. 105*, 155–168. https://doi.org/10.1016/j.isprsjprs.2015.03.014
33. Olofsson P, Foody GM, Herold M, Stehman SV, Woodcock CE, Wulder MA. (2014). Good practices for estimating area and assessing accuracy of land change. *Remote Sensing of Environment. 148*, 42–57. https://doi.org/10.1016/j.rse.2014.02.015
34. Panagos P, Borrelli P, Poesen J, Ballabio C, Lugato E, Meusburger K, Montanarella L, Alewell C. (2015). The new assessment of soil loss by water erosion in Europe. *Environmental Science & Policy. 54*, 438–447. https://doi.org/10.1016/j.envsci.2015.08.012
35. Patel NN, Angiuli E, Gamba P, Gaughan A, Lisini G, Stevens FR, Tatem AJ, Trianni G. (2015). Multitemporal settlement and population mapping from Landsat using Google Earth Engine. *International Journal of Applied Earth Observation and Geoinformation. 35*, 199–208. https://doi.org/10.1016/j.jag.2014.09.005
36. Pelletier C, Valero S, Inglada J, Champion N, Marais Sicre C, Dedieu G. (2017). Effect of training class label noise on classification performances for land cover mapping with satellite image time series. *Remote Sensing. 9*(2), 173. https://doi.org/10.3390/rs9020173
37. Petrosillo I, Valente D, Mulder C, Li B-L, Jones KB, Zurlini G. (2021). The resilient recurrent behavior of Mediterranean semi-arid complex adaptive landscapes. *Land. 10*(3), 296. https://doi.org/10.3390/land10030296
38. Pratson LF, Fay J, Parvathikar S. (2023). Market prospects for biogas-to-energy projects in the U.S.A. based on a techno-economic assessment of major biogas sources in North Carolina. *Sustainable Energy Technologies and Assessments. 60*, 103557. https://doi.org/10.1016/j.seta.2023.103557
39. Roy DP, Wulder MA, Loveland TR, C.e. W, Allen RG, Anderson MC, Helder D, Irons JR, Johnson DM, Kennedy R, et al. (2014). Landsat-8: Science and product vision for terrestrial global change research. *Remote Sensing of Environment. 145*, 154–172. https://doi.org/10.1016/j.rse.2014.02.001
40. Soulard CE, Albano CM, Villarreal ML, Walker JJ. (2016). Continuous 1985–2012 Landsat monitoring to assess fire effects on meadows in Yosemite National Park, California. *Remote Sensing. 8*(5), 371. https://doi.org/10.3390/rs8050371
41. Tamiminia H, Salehi B, Mahdianpari M, Quackenbush L, Adeli S, Brisco B. (2020). Google Earth Engine for geo-big data applications: A meta-analysis and systematic review. *ISPRS Journal of Photogrammetry and Remote Sensing. 164*, 152–170. https://doi.org/10.1016/j.isprsjprs.2020.04.001
42. Weiss M, Jacob F, Duveiller G. (2020). Remote sensing for agricultural applications: A meta-review. *Remote Sensing of Environment. 236*, 111402. https://doi.org/10.1016/j.rse.2019.111402
43. Wulder MA, Loveland TR, Roy DP, Crawford CJ, Masek JG, Woodcock CE, Allen RG, Anderson MC, Belward AS, Cohen WB, et al. (2019). Current status of Landsat program, science, and applications. *Remote Sensing of Environment. 225*, 127–147. https://doi.org/10.1016/j.rse.2019.02.015
44. Xian GZ, Smith K, Wellington D, Horton J, Zhou Q, Li C, Auch R, Brown JF, Zhu Z, Reker RR. (2022). Implementation of the CCDC algorithm to produce the LCMAP Collection 1.0 annual land surface change product. *Earth System Science Data. 14*(1):143–162. https://doi.org/10.5194/essd-14-143-2022
45. Xu F, Somers B. (2021). Unmixing-based Sentinel-2 downscaling for urban land cover mapping. ISPRS *Journal of Photogrammetry and Remote Sensing. 171*, 133–154. https://doi.org/10.1016/j.isprsjprs.2020.11.009
46. Yang J, Huang X. (2021). The 30 m annual land cover dataset and its dynamics in China from 1990 to 2019. *Earth System Science Data. 13*(8), 3907–3925. https://doi.org/10.5194/essd-13-3907-2021
47. Zhang X, Liu L, Chen X, Gao Y, Xie S, Mi J. (2021). GLC_FCS30: global land-cover product with fine classification system at 30 m using time-series Landsat imagery. *Earth System Science Data. 13*(6), 2753–2776. https://doi.org/10.5194/essd-13-2753-2021
48. Zhu Z. (2017). Change detection using Landsat time series: A review of frequencies, preprocessing, algorithms, and applications. *ISPRS Journal of Photogrammetry and Remote Sensing. 130*, 370–384. https://doi.org/10.1016/j.isprsjprs.2017.06.013
49. Zhu Z, Woodcock CE. (2014). Continuous change detection and classification of land cover using all available Landsat data. *Remote Sensing of Environment. 144*, 152–171. https://doi.org/10.1016/j.rse.2014.01.011